한국소음진동공학회 창립10주년 기념 소음진동학술대회논문집, pp. 1493~1510

Statistical Properties of Random Sparse Arrays with Application to Array Design

어레이 설계 응용을 위한 랜덤어레이의 통계적성질

[0]Hyungseok Kook*, Patricia Davies, and J. Stuart Bolton****

ABSTRACT

Theoretical models that can be used to predict the range of mainlobe widths and the probability distribution of the peak sidelobe levels of two-dimensionally sparse arrays are presented here. The arrays are considered to comprise microphones that are randomly positioned on a segmented grid of a given size. First, approximate expressions for the expected squared magnitude of the aperture smoothing function and the variance of the squared magnitude of the aperture smoothing function about this mean are formulated for the random arrays considered in the present study. By using the variance function, the mean value and the lower end of the range i.e., the first 1 percent of the mainlobe distribution can be predicted with reasonable accuracy. To predict the probability distribution of the peak sidelobe levels, distributions of levels are modeled by a Weibull distribution at each peak in the sidelobe region of the expected squared magnitude of the aperture smoothing function. The two parameters of the Weibull distribution are estimated from the means and variances of the levels at the corresponding locations. Next, the probability distribution of the peak sidelobe levels are assumed to be determined by a procedure in which the peak sidelobe level is determined as the maximum among a finite number of independent random sidelobe levels. It is found that the model obtained from the above approach predicts the probability density function of the peak sidelobe level distribution reasonably well for the various combinations of two different numbers of microphones and grid sizes tested in the present study. The application of these models to the design of random, sparse arrays having specified performance levels is also discussed.

1. INTRODUCTION

As described in a previous article [1], it is possible to use a stationary array of microphones to identify the locations and strengths of the noise sources that contribute to an accelerating vehicle's sideline noise level. An unusual feature of that method is that it can be used in the case when the source vehicle moves at a non-constant velocity: during a standard vehicle passby test, for example. In such a test, the position of the vehicle is tracked continuously by using a radar transducer (which measures the vehicle's velocity) and a photoelectric sensor is used to identify the absolute position of the vehicle at one time. From the vehicle's position as a function of time, propagation distances from assumed source locations on a restoration plane (attached to and moving with the side plane of the vehicle) to the stationary array microphones are calculated. Based on those propagation distances, each microphone signal is de-Dopplerized and corrected for the amplitude attenuation resulting from spherical spreading. The processed microphone signals can then be focused on a sequence of locations on the restoration plane to yield the spatial distribution of source strengths at any vehicle position during the passby.

A microphone array to be used for this purpose must satisfy various, sometimes conflicting, requirements. For example, the microphones must be spaced sufficiently closely to avoid spatial aliasing while at the same time the total array aperture must be large enough to allow typical sources to be resolved accurately. To satisfy these requirements by using a fully-populated array suggests the need for an unrealistically large number of microphones, potentially in the thousands.

However, it is known that the conditions listed above may be met by using so-called sparse arrays in which microphones are not placed at all of an aperture's underlying grid locations. In the case of linear sparse arrays, it is known that mainlobe width is essentially the same as that of the equivalent fully-populated array so long as the aperture size of the sparse array is the same as that of the fully-populated array on the underlying grid [2]. Since

*School of Mechanical and Automotive Engineering, Kookmin University, 861-1, Chongnung-dong, Songbuk-gu, Seoul 136-702, Korea
**Ray W. Herrick Laboratories, School of Mechanical Engineering, Purdue University, West Lafayette, IN 47907-1077

the spatial anti-aliasing performance of an array is determined by the minimum spacing in its co-array (i.e., the autocorrelation of the array configuration), sparse arrays possess the same degree of anti-aliasing capability as that of the fully-populated array on the underlying grid. However, it is known that the peak sidelobe levels of sparse arrays tend to be higher than those of equivalent fully-populated arrays. The peak sidelobe level is related to the noise rejection capability of an array and it is usually an important factor by which the performance of an array configuration is assessed. Given that the aperture size and the number of sensors in a linear sparse array are fixed (i.e., that there are sensors placed at both ends of the underlying grid), a broad range of peak sidelobe levels is possible depending on the precise details of the array configuration. Sidelobe levels can to some extent be controlled by applying spatial windows to the array output. However, the possibility of applying spatial windows to reduce the peak sidelobe levels has been excluded in the present study since the weighting factors for each microphone are assumed to be related to the propagation distances from each point of interest on the restoration plane to each microphone [1].

Two methods are frequently used to design linear arrays having an equi-spaced, linear grid: they result in either minimum redundant or non-redundant linear arrays. The design of minimum redundant linear arrays is described in Moffet [3], and Panayirci and Chen [4]. In the case of a minimum redundant array, the number of redundancies in the co-array is minimized subject to the restriction that there should be no "holes", or zero correlation values, within the array's co-array. Non-redundant linear arrays are described in Vertatschitsch and Haykin [5]: their co-arrays have only zero or unit correlation values (except at zero lag). While a non-redundant array usually yields the largest aperture amongst the possible array types given a fixed number of sensors, the "holes" in the co-array result in sidelobe levels that are likely to be higher than those resulting from the use of a minimum redundant array. The benefit of minimum redundant and non-redundant arrays given a certain number of sensors is that they result in a relatively large aperture size without unnecesary loss in baselines, thus allowing good spatial resolution (i.e., small mainlobe width) to be obtained. However, given the maximum aperture size and the available number of sensors, the question is: Are minimum redundant or non-redundant array the optimal sparse arrays in the sense that they also yield the smallest peak sidelobe level amongst all possible sparse arrays that extend over the same aperture size?

In the case of two-dimensional sparse arrays, these linear array design methods cannot be easily extended. Moreover, it is not even easy to define an array's "aperture size". There have been relatively few publications related to the design of two-dimensional arrays. One approach to designing two-dimensional arrays was suggested by Klemperer [6]. In his method, non-redundant arrays were generated based on a six-sensor array of zero-redundancy to which three sensors at a time were added axisymmetrically on a triangular grid. Among the non-redundant arrays generated, the best array configuration was selected based on the criteria of "compactness" and large "core number", the latter being defined as the total number of baselines in the central portion of the co-array within a limiting circle in which just a small proportion (5 to 10 percent) of holes was allowed. However, this method cannot be used for design of non-axisymetrical arrays (for instance, rectangular arrays) in applications where such arrays are preferred. Klemperer's method represents an extension to two dimensions of the philosophy that the array having the smallest number of redundancies will be the best amongst the possible array configurations that could be constructed on the underlying grid.

Another two-dimensional array design method involves the generation of arrays in which sensors are positioned randomly within a given aperture region. The positioning of sensors in a random fashion helps to avoid the periodicity inherent in non-random arrangements, thus possibly flattening the co-array values. Random arrays are essentially extreme versions of non-redundant arrays when a large enough number of sensors are involved. However, to justify the use of array design methods based on minimizing the number of redundancies, it should first be demonstrated that an array having a small number of redundancies generally yields small peak sidelobe levels. Another feature of random arrays is that arrays generated by other design methods, e.g., crossed arrays [7] and elliptically spiral array [2], are all subsets of random arrays so long as they all share the same underlying grid. Therefore, without restricting the shape of the arrays, it may be considered wise to let a best array (satisfying both the mainlobe width and the peak sidelobe requirements) be selected through exhaustive search of a population of random arrays.

In practice, the specification of two-digit numbers of grid points in both horizontal and vertical directions (for example, 80×40) in a rectangular aperture to be populated sparsely by a manageable number of sensors (for example, 64) would yield a very large number of possible array configurations. The subset of arrays that can be tested even given a large period of computation generally amounts to small fraction of the total set of arrays. Therefore it would be of benefit when determining the number of sensors and the grid size to be used in a particular application if the ranges of mainlobe widths and peak sidelobe levels of various classes of random array configurations could be estimated before starting a time-consuming search process.

In relation to this topic, Lo [8] developed an approximate method of determining the critical number of sensors required to generate a random linear array having a specified peak sidelobe level with a good chance of success. Lo's approximate method is based on a statistical approach and is asymptotically valid for large numbers of sensors (in his study, cases where the number of sensors were greater than 100 were considered).

In the present paper, a similar tool that can be used even in the case of a relatively small number of microphones is described. The model presented in the present study can predict the range of distributions of the mainlobe widths and the probability distributions of peak sidelobe levels of randomly generated two-dimensional arrays given the grid size and the number of microphones to be positioned on the grid. In principle, the method presented here can be used to predict the smallest possible mainlobe width and the lowest possible peak sidelobe levels obtainable within, for instance, a few thousands trials for various grid sizes. Thus, one can use the present tools to choose an appropriate grid size and spacing given a specified number of sensors before a time consuming exhaustive search is performed. Alternatively, these tools can be used to estimate the minimum number of sensors that is necessary to meet specified requirements for peak sidelobe level, mainlobe width and anti-aliasing performance.

In any particular instance, a carefully designed array configuration may perform better than the best of a set of randomly generated array configurations in terms of peak sidelobe level and mainlobe width. However it is generally not an easy task to design an array as the number of microphones increases. Even in the case where one attempts to design an array configuration according to some set of criteria, the tools that are described in the present article can be used to establish a standard against which the peak sidelobe levels and the mainlobe width of those array configurations can be compared. As benchmarking studies, the problem of placing 16 and 64 microphones within different sized square apertures is also considered here.

2. RANDOM ARRAY GENERATION WITH A SEGMENTING SCHEME

2.1. GRID SPACING

Given a specified aperture in the x-z plane, the fundamental grid spacing in the x and z-directions (i.e., in the horizontal and vertical directions, respectively) is determined by the spatial anti-aliasing capability required in a specific application. For vehicle passby applications, the fundamental grid spacing is determined by the frequency range of interest and the maximum incidence angle from the noise sources to the center of the array. Standard motor vehicle passby test procedures are described in ISO 362-1981. Here it is assumed that it is desired to identify the source locations and strengths over a vertical plane extending from −10 m to 10 m from the center of the array and horizontally separated from the array: see Figure 1. Then the maximum incidence angle occurs when the vehicle is either at the entrance or exit of the test section as depicted in Figure 1. To avoid spatial aliasing, it is required that there be at least two sensor spacings, $2d$ within one spatial cycle of the sound field in the x-direction. Therefore, the maximum sensor spacing, d_x, that is allowed in the x-direction can be calculated as:

$$d_x = \frac{c}{2 f_{max} \sin\theta}. \qquad (1)$$

For instance, when the frequency range of interest is 500 Hz to 2 kHz, d_x is calculated to be about 0.107 m. The above analysis assumes the existence of a plane phase plane (i.e., a far field source). However in reality, the noise sources on the restoration plane (i.e., the side plane of the vehicle) lie within the "near field" of the microphone array i.e., spherical spreading effects are significant. A similar analysis performed assuming spherical phase planes would generally result in a decrease in the allowable sensor spacing in the x-direction; an exact analysis would require a knowledge of the microphone positions *a priori*. Therefore the sensor spacing in the x-direction should be selected so that it is smaller than the value calculated above, and the appropriateness of the spacing should be checked after the array design is finalized.

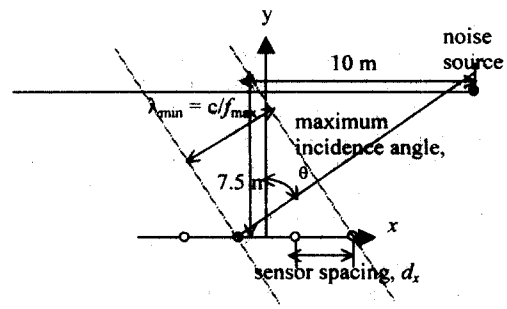

Figure 1: Determination of maximum allowable sensor spacing in the x-direction (the direction of vehicle movement).

2.2. SEGMENTING SCHEMES

Once the grid spacing is determined for a regular grid, all the sparse arrays on the same underlying grid share the same spatial aliasing characteristics except in the case of sparse arrays in which microphones happen to be placed at integer multiples of the underlying grid spacing (i.e., where

the actual microphone spacing is an integer multiple of the nominal grid spacing). The mainlobe width and the peak sidelobe level of a sparse array then depend on the aperture size and the way the microphones are disposed on the grid points.

The mainlobe width in particular is strongly related to the aperture size of an array configuration (that relation will be discussed in detail in subsection 3.2). The aperture sizes of random arrays, and thus the mainlobe width, can be controlled by specifying the underlying grid size. However, when numbers of sensors are positioned randomly on the grid, sensors can clump together in a small region thus yielding a smaller effective aperture size than is suggested by the nominal grid size. To make sure that the sensors are spatially well distributed after an appropriate grid size is fixed, schemes based on segmenting the whole aperture into smaller subsections were considered in the present study.

In a segmenting method, sensors are first grouped on a segment-by-segment base, and each group of sensors is then positioned randomly within each subsection as in the random array design method. Moebs [9] first used a segmenting scheme when designing a 16-microphone array to resolve the problem that sensors can tend to clump together in a small region when their positions are chosen randomly. In his case, he segmented a rectangular aperture into 3×3 subsections of equal width and height. In his method, one microphone was always positioned at the center of the array's aperture and the rest of the microphones were positioned randomly within the various subsections.

Figure 2 shows three segmenting schemes for a square, 12×12 grid. Since the width and height of the 12×12 grid is 1 m × 1 m, the grid spacing, d_x and d_z, is approximately 0.09 cm, which is short enough to spatially resolve a wavelength at the upper frequency limit, 2 kHz, at which noise levels in vehicle passby tests are most significant [9]. To study the effects of segmenting the baseline grid into uniform subsections, the baseline aperture (denoted segmenting scheme 1) shown in Figure 2(a) was uniformly divided into 2×2 subsections and 4×4 subsections as shown in Figures 2(b) and (c), and they will be referred to here as segmenting schemes 2 and 3, respectively. As the number of the uniform subsections increases, microphones tend to spread evenly over the grid.

The mainlobe widths and peak sidelobe levels of array configurations can be estimated from the squared magnitude of their aperture smoothing functions where the aperture smoothing function, $W(\vec{k})$, is defined as:

$$W(\vec{k}) = \sum_{r}^{M} \exp(j\vec{k} \cdot \vec{x}_r). \qquad (2)$$

In Equation (2), $\vec{x}_r$ and $\vec{k}$ denotes the r-th sensor's position vector and the wave number vector, respectively. Therefore the aperture smoothing function represents the two-dimensional spatial Fourier transform of the microphone's positions.

For each array configuration generated, the squared magnitude of the aperture smoothing function was calculated using a zero-padded 96×96-point FFT. Figure 3 shows an example of the squared magnitude of an aperture smoothing function generated using segmenting scheme 2 for sixteen microphones. From the squared magnitude of the aperture smoothing function, the mainlobe widths based on the 3 dB-down contour lines and peak sidelobe levels were calculated as shown in Figure 3. Note that the present work is concerned with two-dimensional array configurations and "mainlobe width" in the present article in fact represents the mainlobe "area" which therefore has the unit of m^{-2} (area in the wave number domain).

Two thousand array configurations were randomly generated by using each segmenting scheme, and the 3-dB down mainlobe widths and the peak sidelobe levels in each case are plotted in Figures 4(a), (b), and (c), respectively. The best choice of an array configuration from amongst all the random arrays would be the array configuration that yielded the smallest mainlobe width and the lowest peak sidelobe level. it can be seen in Figures 4(a), (b), and (c) that an appropriate choice of an array configuration is from those at the lower bound of the distributions: that is, from those arrays having the smallest possible mainlobe bandwidth for the same peak sidelobe level.

When segmenting schemes 2 and 3 are considered (2×2 and 4×4 uniform subsections, respectively), it can be seen from Figures 4(b) and (c) that the lower bound of the mainlobe width did not change significantly from the lower bound shown in Figure 4(a); the variation of the mainlobe width distribution was decreased, however. The array configurations distributed within the upper portion of Figure 4(a) are presumably those array configurations that have much smaller aperture sizes than the nominally specified aperture size. Therefore, the introduction of uniform segmenting schemes in the generation of random arrays helps to filter out array configurations having relatively large mainlobe widths for the same peak sidelobe level without losing those array configurations at the lower bound. For this reason, it was decided to use the uniform 2×2 segmenting scheme in the present work (since segmenting scheme 3 may be too restrictive). The random array configurations investigated in the present study were generated based on segmenting scheme 2, unless stated otherwise.

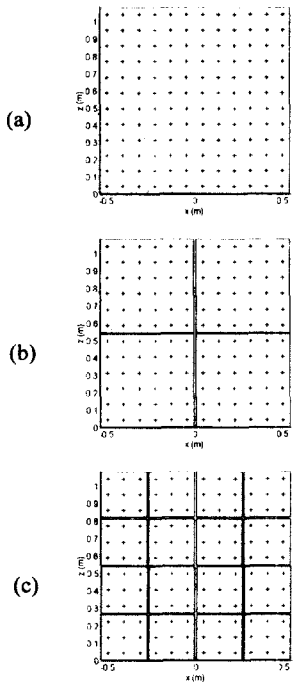

Figure 2: Square array apertures and uniform segmenting schemes. Gray regions represent subsections and the underlying grid points in each subsection are denoted by '+' symbols. The segmented array apertures shown in (a), (b), and (c) are denoted segmenting schemes 1, 2, and 3, respectively.

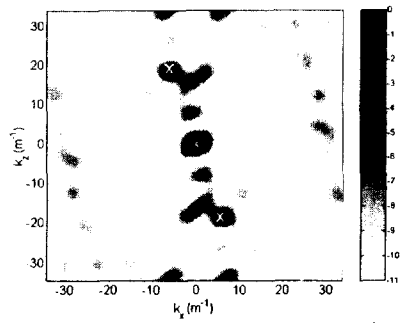

Figure 3: An example of the squared magnitude of the aperture smoothing function of an array generated using segmenting scheme 2. The x at the center of the plot represents the peak of the mainlobe and the other two x's represent the peak sidelobes. The closed curve at the mainlobe location shows the 3 dB-down contour line. The scale bar represents a decibel scale.

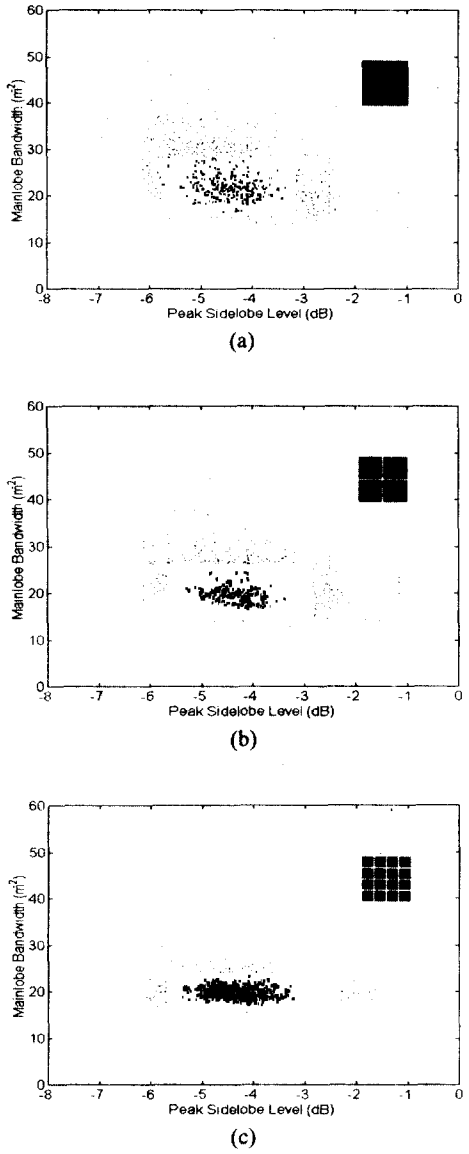

Figure 4: Correlation between the peak sidelobe levels and the 3 dB-down bandwidths of sets of 2,000 randomly generated arrays generated using (a) segmenting scheme 1, (b) segmenting scheme 2, and (c) segmenting scheme 3.

3. THEORETICAL MODEL AND RESULTS

3.1. MEAN AND VARIANCE OF THE APERTURE SMOOTHING FUNCTION

The expected value and the variance of the squared magnitude of the aperture smoothing function for random arrays were investigated next. These quantities have been discussed in reference [10] for random arrays created without use of a segmenting scheme. In that work, sensors were assumed to be distributed over a predefined aperture without an underlying grid. Sensors were placed randomly and independently of each other without regard to the positions of previously positioned sensors. In the present study, the formulae for the expected value and the variance of the squared magnitude of the aperture smoothing function are generalized so as to make it possible to deal with cases in which segmenting schemes are used. Even though the present discussion is restricted in detail to the case of a uniform 2×2 segmenting scheme, the formulae which will be presented here can be applied to general segmenting schemes comprising any number of arbitrarily shaped subsections. The only constraint that is imposed in the derivation procedure is that the same number of sensors should be assigned to each subsection.

In the procedure that follows, it was assumed that sensors could be placed continuously within each subsection without regard to the predefined grid points in order to simplify the analysis. The squared magnitude of the aperture smoothing function of array configurations composed of M sensors can be expressed as [10]:

$$\left|W(\vec{k})\right|^2 = \sum_{r_1, r_2}^{M} \exp\left\{j\vec{k}\cdot(\vec{x}_{r_1} - \vec{x}_{r_2})\right\}, \tag{3}$$

where $\vec{x}_r$ and $\vec{k}$ denotes the r-th sensor's position vector and the wave number vector, respectively.

The expected squared magnitude of the aperture smoothing function for random array configurations can then be expressed as:

$$\mathrm{E}\left[\left|W(\vec{k})\right|^2\right] = \sum_{r_1, r_2}^{M} \mathrm{E}\left[\exp\left\{j\vec{k}\cdot(\vec{x}_{r_1} - \vec{x}_{r_2})\right\}\right]. \tag{4}$$

The latter summation can be divided into the case where $r_1 = r_2$, and the case in which $r_1 \neq r_2$: that is,

$$\mathrm{E}\left[\left|W(\vec{k})\right|^2\right] = M + \sum_{r_1 \neq r_2}^{M} \mathrm{E}\left[\exp\left\{j\vec{k}\cdot(\vec{x}_{r_1} - \vec{x}_{r_2})\right\}\right]. \tag{5}$$

Moreover, the case where $r_1 \neq r_2$ can be further classified into the case in which the two different sensors, r_1 and r_2, lie within the same sub-section and the case in which they lie within two different sub-sections: i.e.,

$$\mathrm{E}\left[\left|W(\vec{k})\right|^2\right] = M + \sum_{p}^{n} \sum_{r_1 \neq r_2}^{m(m-1)} \mathrm{E}\left[\exp\left\{j\vec{k}\cdot(\vec{x}_{r_1} - \vec{x}_{r_2})\right\}\right] + \sum_{p \neq q}^{n} \sum_{r_1 \neq r_2}^{m^2} \mathrm{E}\left[\exp\left\{j\vec{k}\cdot(\vec{x}_{r_1} - \vec{x}_{r_2})\right\}\right] \tag{6}$$

In Equation (6), n and m, respectively, denote the number of subsections and the number of microphones within each subsection: the latter quantity is $m = M/n$. The variables p and q are integer values denoting the index number of the subsections. The second term corresponds to the former case in which the two different sensors r_1 and r_2 are within the same subsection while the third term corresponds to the case in which they are within two different subsections. Since the random variables $\vec{x}_{r_1}$ and $\vec{x}_{r_2}$ are independent of each other, Equation (6) can be simplified to:

$$\mathrm{E}\left[\left|W(\vec{k})\right|^2\right] = M + m(m-1)\sum_{p}^{n} \Phi_p(\vec{k})\Phi_p(-\vec{k}) + m^2 \sum_{p \neq q}^{n} \Phi_p(\vec{k})\Phi_q(-\vec{k}) \tag{7}$$

where $\Phi_p(\vec{k})$ is the characteristic function of the random variable governing sensor placement in sub-section p, defined as $\Phi_p(\vec{k}) = \mathrm{E}\left[\exp\left\{j\vec{k}\cdot\vec{x}\right\}\right]$, and $\Phi_p(-\vec{k})$ denotes its complex conjugate. Equation (6) can be manipulated to yield an alternate form: i.e.,

$$\mathrm{E}\left[\left|W(\vec{k})\right|^2\right] = M + m^2 \sum_{p,q}^{n} \Phi_p(\vec{k})\Phi_q(-\vec{k}) - m\sum_{p}^{n} \Phi_p(\vec{k})\Phi_p(-\vec{k}). \tag{8}$$

Next, the variance of the squared magnitude of the aperture smoothing function about the expected value can be obtained from the following formula [10]:

$$\sigma^2 = \mathrm{E}\left[\left|W(\vec{k})\right|^4\right] - \mathrm{E}\left[\left|W(\vec{k})\right|^2\right]^2, \tag{9}$$

where the expected value of the fourth power of the magnitude of the aperture smoothing function is

$$\mathrm{E}\left[\left|W(\vec{k})\right|^4\right] = \sum_{r_1, r_2, r_3, r_4}^{M} \mathrm{E}\left[\exp\left\{j\vec{k}\cdot(\vec{x}_{r_1} - \vec{x}_{r_2} + \vec{x}_{r_3} - \vec{x}_{r_4})\right\}\right]. \tag{10}$$

A similar but more tedious procedure than that used to obtain Equation (8) yields an equation for the fourth power of the magnitude of the aperture smoothing function: i.e.,

$$
\begin{aligned}
\mathrm{E}\left[\left|W\left(\vec{k}\right)\right|^4\right] &= M(2M-1)+4m^2(2m-1+m(n-2)u_3) \\
&\times \sum_{p,q}^{n} \Phi_p\left(\vec{k}\right)\Phi_q\left(-\left(\vec{k}\right)\right)+4m\left(m^2(n-2)(1-u_3)-mn+1\right) \\
&\times \sum_{p}^{n} \Phi_p\left(\left(\vec{k}\right)\right)\Phi_p\left(-\left(\vec{k}\right)\right) \\
&+ 2u_3m^3\,\mathrm{Re}\left\{\sum_{p,q,r}^{n} \Phi_p\left(2\left(\vec{k}\right)\right)\Phi_q\left(-\left(\vec{k}\right)\right)\Phi_r\left(-\left(\vec{k}\right)\right)\right\} \\
&- 4m^2(m(u_3-1)+1)\mathrm{Re}\left\{\sum_{p,q}^{n} \Phi_p\left(2\vec{k}\right)\Phi_p\left(-\vec{k}\right)\Phi_q\left(-\vec{k}\right)\right\} \\
&- 2m^2(m(u_3-1)+1)\mathrm{Re}\left\{\sum_{p,q}^{n} \Phi_p\left(2\vec{k}\right)\Phi_q^2\left(-\vec{k}\right)\right\} \\
&+ 4m(m^2(u_3-1)+1)\mathrm{Re}\left\{\sum_{p}^{n} \Phi_p\left(2\vec{k}\right)\Phi_p^2\left(-\vec{k}\right)\right\} \\
&+ m^2\sum_{p,q}^{n} \Phi_p\left(2\vec{k}\right)\Phi_q\left(-2\vec{k}\right)-m\sum_{p}^{n} \Phi_p\left(2\vec{k}\right)\Phi_p\left(-2\vec{k}\right) \\
&+ u_3m^4 \sum_{p,q,r,s}^{n} \Phi_p\left(\vec{k}\right)\Phi_q\left(-\vec{k}\right)\Phi_r\left(\vec{k}\right)\Phi_s\left(-\vec{k}\right) \\
&+ 4m^3(m(u_3-u_4)-u_3) \\
&\times \sum_{p,q,r}^{n} \Phi_p\left(\vec{k}\right)\Phi_p\left(-\vec{k}\right)\Phi_q\left(\vec{k}\right)\Phi_r\left(-\vec{k}\right) \\
&+ 2m^3(m(u_3-u_4)-u_3) \\
&\times \mathrm{Re}\left\{\sum_{p,q,r}^{n} \Phi_p\left(\vec{k}\right)\Phi_p\left(-\vec{k}\right)\Phi_q\left(\vec{k}\right)\Phi_r\left(-\vec{k}\right)\right\} \\
&+ 4m^2\left((m-1)(m-2)-u_4m^2-3m(m(u_3-u_4)-u_3)\right) \\
&\times \mathrm{Re}\left\{\sum_{p,q}^{n} \Phi_p\left(\vec{k}\right)\Phi_p\left(-\vec{k}\right)\Phi_p\left(\vec{k}\right)\Phi_q\left(-\vec{k}\right)\right\} \\
&+ 2m^2\left((m-1)^2-u_4m^2-2m(m(u_3-u_4)-u_3)\right) \\
&\times \sum_{p,q}^{n} \Phi_p\left(\vec{k}\right)\Phi_p\left(-\vec{k}\right)\Phi_q\left(\vec{k}\right)\Phi_q\left(-\vec{k}\right) \\
&+ m^2\left((m-1)^2-u_4m^2-2m(m(u_3-u_4)-u_3)\right) \\
&\times \sum_{p,q}^{n} \Phi_p^2\left(\vec{k}\right)\Phi_q^2\left(-\vec{k}\right) \\
&+ 6m\left(2m^2u_3(m-1)-m^3u_4-(m-1)(m^2-m-1)\right) \\
&\times \sum_{p}^{n} \Phi_p^2\left(\vec{k}\right)\Phi_p^2\left(-\vec{k}\right)
\end{aligned} \tag{11}
$$

where u_a denotes unit step function defined as:

$$
u_a = \begin{cases} 1, & (n \geq a) \\ 0, & (\text{otherwise}). \end{cases} \tag{12}
$$

Equations (8) and (11) can easily be evaluated provided that the probability density functions of the random variable (the sensor's position vector $\vec{x}$, in this application) are defined for each subsection. The gray regions in Figure 2 represent the subsections. Note that the corresponding subsections are larger than the grid size in each sub-section (so that the average aperture size of the continuous array configurations is equal to that of the discrete array configurations).

Figure 5(a) shows the expected squared magnitude of the aperture smoothing functions of random arrays based on segmenting scheme 2 with a grid size of 12×12, when a uniform probability density function was assumed to apply in each subsection. Figures 5(b) and (c) show the $\pm 2\sigma$ variations of the expected squared magnitude of the aperture smoothing functions about this mean. A cross-sectional view of Figure 5 along the line $k_z = 0$ is shown in Figure 6 along with results calculated for other sets of random arrays generated by using different grid sizes. The grid sizes used to generate the data shown in Figures 6(a), (b), and (c) were 4×4, 6×6, and 12×12, respectively. Each complete grid was divided into uniform 2×2 subsections (segmenting scheme 2), and zero-padded 32×32, 48×48, and 96×96-points FFT's were used, respectively, to calculate the squared magnitudes of the aperture smoothing functions for 2,000 randomly generated array configurations for each grid size (except for the case of a 4×4 grid, when only a single configuration is possible). In the figures, the predicted expected squared magnitude of the aperture smoothing function is denoted by a solid line, while the predicted variations ($\pm 2\sigma$) about this mean are denoted by dashed lines. The dots represent the corresponding curves calculated on the basis of the 2,000 randomly generated array configurations.

It can be seen that the simulation results show progressively better agreement with the predictions of the theory as the grid size becomes larger. This follows because Equations (8) and (11) were derived based on the assumptions that sensors could be placed on the aperture continuously (i.e., without a grid), and that sensors are positioned randomly without regard to the previously positioned sensors. However, in the simulation, placing more than one microphones at the same grid point was not allowed, and sensors were positioned on discrete grid points. Therefore, the theoretical model does not account for the effects of grid size, and predicts identical expected means and variances regardless of the grid spacing so long as the aperture size is the same. However, it should be noted that the grid size effect exists in practice: as the grid

size becomes smaller, the discrepancies between the predicted values and the results obtained from simulated array configurations increase. For the case of a 6×6 grid (see Figure 6(b)), the mean value was overestimated, especially near the minima of the squared magnitude of the aperture smoothing function, by approximately 2-3 dB. Also note that the variances tend to be overestimated compared to the actual values as the grid size becomes smaller. For the case of a 4×4 grid, in which case, a fully-populated, unique sixteen microphone array configuration exists, the theory cannot predict the variance of the squared magnitude of the aperture smoothing function. Therefore, the theoretical model presented in this subsection for the expected squared magnitude of the aperture smoothing function and the corresponding variance become asymptotically exact as the grid size becomes larger.

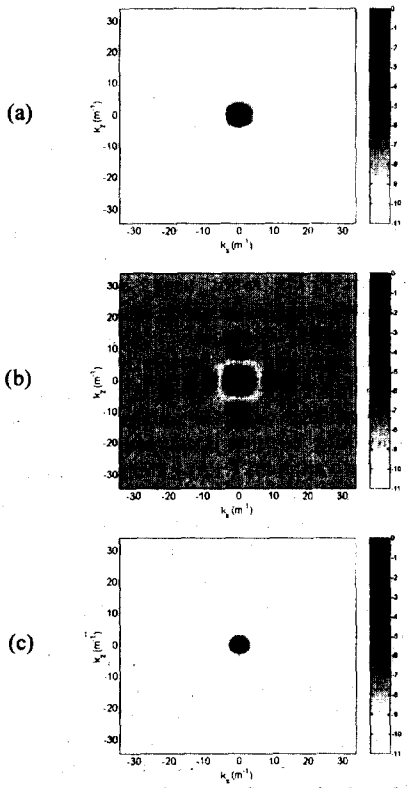

Figure 5: Expected squared magnitude of the aperture smoothing function and ±2σ variations about this mean calculated for random arrays generated by using the segmenting scheme 2; (a) expected value; (b) +2σ variation; (c) -2σ variation. Scale bar denotes a decibel scale.

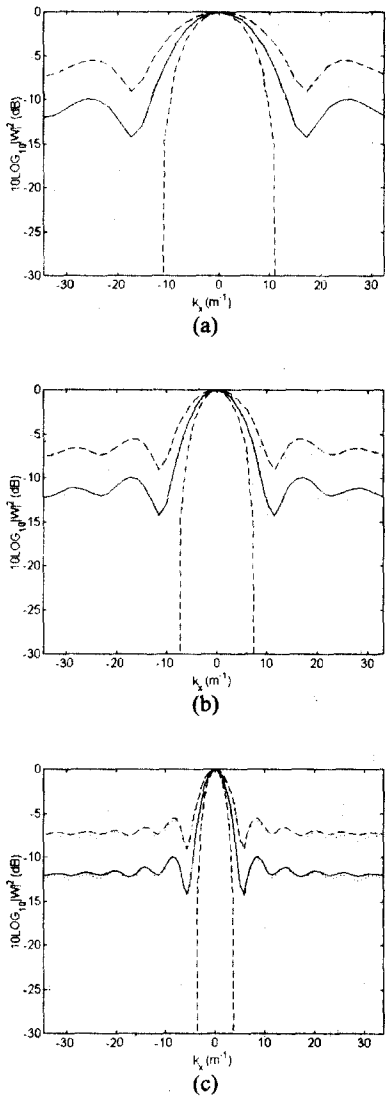

Figure 6: Cross-sections (k_z = 0) of the expected squared magnitude of the aperture smoothing function (solid line) and the variation (±2σ) about this mean (dashed lines) calculated for random arrays generated using the segmenting scheme 2. Dotted lines denote the expected values and the variances of the squared magnitude of the aperture smoothing function, respectively, obtained by averaging results from 2,000 randomly generated arrays with the same segmenting scheme; (a) 4×4 grid, (b) 6×6 grid, (c) 12×12 grid.

3.2. MAINLOBE WIDTHS AND EFFECTIVE APERTURE SIZES

It is known that an array's mainlobe width is generally dependent on its aperture size. For linear arrays, the aperture size is simply the distance from one end of the array to the other. In this subsection, the relationship between the mainlobe width and the "size" of two-dimensional array configurations is investigated based on observations of random arrays generated for different segmenting schemes, grid sizes, and numbers of microphones.

There is no concrete definition of "aperture size" for two-dimensional arrays, but since aperture size in linear arrays is approximately proportional to the degree to which the microphones are spread out, it was of interest to investigate the correlation between the polar moments of an array's microphone positions and its mainlobe width.

In Figure 7, mainlobe widths are plotted as a function of array polar moments for five sets of 2,000 random arrays generated by using the three different segmenting schemes, three different grid sizes, and two different numbers of microphones. That is, for 16-microphone arrays, the segmenting schemes 1, 2, and 3 used in combination with a 12×12 grid size were tested; a different grid size, 6×6 used, in combination with segmenting scheme 2, was also tested. To test a case involving a different number of microphones, 64-microphone arrays were generated by using a 24×24 grid size based on segmenting scheme 2.

The grid spacing in both the x- and z-directions was 1/11 m for all array configurations. In Figure 7, the vertical axis represents the polar moment per sensor while the horizontal axis denotes the square root of the mainlobe width. The distributions of the polar moments per sensor and the roots of the mainlobe widths of the array configurations can be seen to approximately follow the curve $y = 1.87/x$, regardless of segmenting scheme, grid size, or the total numbers of sensors.

The hyperbolic relationship between the polar moment per sensor and the root of mainlobe width observed for two-dimensional arrays may be explained by analyzing linear, regular (i.e., fully-populated) arrays. Consider, a linear regular array composed of M sensors with sensor spacing, d. The mainlobe bandwidth of the linear array is [10]:

$$x = 4\pi/Md. \tag{13}$$

Here, the mainlobe width is not the 3 dB-down bandwidth, but the "zero-crossing" bandwidth. The moment of the microphone positions with respect to the mass center of the array can be easily calculated, and it is $M^2d/4$ and $(M^2-1)d/4$ for even and odd values of M, respectively. Therefore the moment per sensor can be approximated as:

$$y = Md/4. \tag{14}$$

Note that Equation (14) yields negligible error even when M is a relatively small number (for example, there is a 4 percent error for the case $M = 5$). From Equations (13) and (14), the moments per sensor can be related to the mainlobe widths for the case of linear regular arrays: i.e.,

$$y = \pi/x. \tag{15}$$

Note that variables M and d do not appear in Equation (15).

In the case of two-dimensional regular arrays, it can be shown that the above result can be applied in both the x- and z-directions, independently: i.e., the moments of microphone positions about the $z = 0$ and $x = 0$ axes (provided that the mass center of an array is positioned at $z = 0$ and $x = 0$) determine the mainlobe width in the k_x and k_z directions, respectively.

Note that the above procedures were derived for fully-populated arrays. However, it is shown in Figure 7 that the hyperbolic relation between the mainlobe widths and the moment per sensor still holds for sparse arrays. In Figure 7, the root of the mainlobe width (in fact, the root of the mainlobe "area", which has the same dimension as the mainlobe width in linear arrays) was used as the scale for the horizontal axis and instead of investigating the relationships in the x- and z-directions independently, the polar moment was used as the scale of the vertical axis since the shape of the apertures were square in the present case. The constant in the hyperbolic curve used to fit the data is 1.87: i.e.,

$$y = 1.87/x. \tag{16}$$

This constant is universal in the sense that it is independent of the grid spacing and the number of sensors.

The agreement between the data and the fitted curve seems to be good at least for the array configurations generated by using segmenting schemes that ensure a degree of "squareness" of the distributions of the microphones: small amount of deviations from the hyperbolic relationship can be observed for some array configurations generated from segmenting scheme 1 that does not impose any restrictions on the microphone placement (note that the distributions of the 16-microphone random arrays generated by using a 12×12 grid based on segmenting scheme 1, 2, and 3, respectively, is illustrated by means of a sketch in Figure 7). Based on the present simulations and analysis, it is also believed that the mainlobe widths of linear sparse arrays depend strongly on the moments of the arrays' microphone positions, even though this dependency has not been rigorously investigated in the present study.

It was shown in reference [2] that elliptical arrays generally have smaller mainlobe widths than do random

arrays even when the latter have relatively larger aperture sizes. That observation can be explained in terms of the array polar moment. Even though the nominal array aperture sizes defined by the area within the envelope of the array configurations of elliptical arrays are generally smaller than those of random arrays generated on the rectangular aperture enclosing the elliptical arrays, the corresponding polar moment of the elliptical array configurations can be larger since all of the microphones are positioned around the edges of the array envelope.

Therefore, it is concluded here that the polar moment of microphone positions with respect to the center of the microphone array can be used as a measure for the equivalent array aperture size in the case of two-dimensional arrays (moments about the x- and z-axes determine the mainlobe width in the z- and x-directions, respectively, in the more general case of non-square apertures). For instance, Equation (14) may be used in defining the equivalent aperture lengths of a two-dimensionally sparse array configuration in the x- and z-directions, respectively. That is, from the fact that the aperture size of a linear regular array is approximately four times the moment per sensor of the linear regular array, the lengths of the equivalent aperture size of a two-dimensional array configuration in the x- and z-directions, respectively, can be defined as four times the moments of the sensors about the z- and x-axes, respectively.

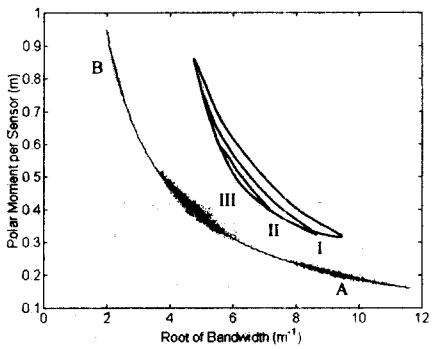

Figure 7: Correlations between the roots of the mainlobe bandwidths and the "polar moment per sensor" of 16-microphone random array configurations and 64-microphone array configurations. The 16-microphone random arrays generated based on segmenting schemes 1, 2, and 3 and with the grid size 12×12 are denoted by I, II, and III. The 16-microphone random arrays based on segmenting scheme 2 with a grid size 6×6 are denoted by A. 64-microphone random array configurations generated based on segmenting scheme 2 with the grid size 24x24 are denoted by B. Data points were curve-fitted (shown as a solid line) by using the formula, $y = 1.87/x$.

3.3. RANGE OF THE MAINLOBE WIDTH DISTRIBUTION

The formulae for the expected value and variance of the squared magnitude of the aperture smoothing function do not give direct information about the statistical properties of the mainlobe widths or the peak sidelobe levels. In the present subsection, an approximate method that can be used to predict the range of the most likely mainlobe widths (i.e., that fall within the 1 percent to 99 percent range of the cumulative distribution) will be described.

A probability density function for the distribution of the 3-dB down mainlobe widths was obtained based on 20,000, 16-microphone array configurations that were randomly generated on a square 12×12 grid using segmenting scheme 2 and a grid spacing of 1/11 m: the probability density function is shown in Figure 8 where the cumulative distribution (in two forms) is also shown above the bar graph. The probability density function for the distribution of the mainlobe widths was observed to be skew-symmetric. Here the object was not to identify an appropriate probability distribution model for the distribution of mainlobe widths, but to find an approximate method for predicting the range of the mainlobe widths within which fall most of the 3-dB down mainlobe widths.

As shown in Figures 6(a), (b), and (c), the variance of the squared magnitude of the aperture smoothing function from the expected value is large in the sidelobe regions. However, the variance of the squared magnitude of the aperture smoothing function is small around the mainlobe (it is zero at $k_x = k_z = 0$), and therefore information about the mainlobe widths can be well estimated by using Equations (8) and (11). The mean value and the plus and minus variation of the mainlobe 3 dB-down (half-power) bandwidth can be obtained by contouring the mean and variance surfaces of the squared magnitude of the aperture smoothing function at the –3 dB plane and by calculating the areas within those intersecting curves. By following this procedure, the variance of the mainlobe width was estimated and is marked on the upper of the two horizontal lines in Figure 8. Mainlobe widths were calculated by using the squared magnitude of the aperture smoothing functions varied by $\pm 2.5\sigma$, $\pm 1.5\sigma$, $\pm 0.5\sigma$ from the expected squared magnitude of the aperture smoothing function. The expected squared magnitude of the aperture smoothing function and the standard deviation, σ , as a function of the wave number can be obtained by using Equations (8) and (9), respectively. Note that the mainlobe widths that correspond to $\pm 2.5\sigma$, $\pm 1.5\sigma$, $\pm 0.5\sigma$ are not positioned symmetrically with respect to the mean value of the mainlobe width PDF (i.e., the mainlobe width that corresponds to $\sigma = 0$). This follows since the mainlobe

width is the horizontal area formed on a plane parallel with the wave number domain, while the plus and minus variations in the expected square magnitude of the aperture smoothing function is obtained by vertically adding and subtracting the multiplied standard deviation to and from the expected squared magnitude of the aperture smoothing function. The lower of the two horizontal lines above the bar graph represents the cumulative distributions of the mainlobe widths that were obtained from the probability distributions of the latter.

Note that the mainlobe width associated with $-1.5\ \sigma$ is approximately the same as that associated with the first one percent of the total distribution. However, the mainlobe width associated with $+1.5\ \sigma$ does not correspond to the mainlobe width associated with the last one percent of the total distribution, and it can be seen that the last one percent of the array configurations have mainlobe widths associated with the deviations lying between $1.5\ \sigma$ and $2.5\ \sigma$. However, here we are primarily concerned with narrow mainlobe widths.

To see if the one percent mainlobe width is well predicted by calculating the mainlobe width for $-1.5\ \sigma$ variations in the squared magnitude of aperture smoothing function for other grid sizes and the number of microphones, 2,000 random arrays were generated for each of 9 different grid sizes for the case of a 16-microphone array designed according to segmenting scheme 2 and having a grid spacing of 1/11 m. The grid sizes considered here were 4×4, 5×5, 6×6, 7×7, 8×8, 12×12, 16×16, 24×24, and 48×48. For the case of 64-microphone arrays, a further 2,000 random arrays were generated in a similar manner for 10 different grid sizes: 8×8, 9×9, 10×10, 12×12, 16×16, 20×20, 24×24, 28×28, 48×48, and 72×72. Note that for the cases of 5×5, 7×7 for the 16-microphone arrays and for the case of 9×9 for the 64-microphone arrays the whole grid cannot be divided evenly due to the odd numbers of grid points in the x and z-directions: thus the grid was horizontally divided below the central row and vertically divided left of the central column of the grid. For each array realized in this way, a zero–padded FFT with the number of points in each direction eight times greater than the given nominal array size was used to evaluate the 3-dB down mainlobe widths.

Since the lower end of the mainlobe width distribution is of prime concern, the range of mainlobe widths associated with $\pm 1.5\,\sigma$ deviations were calculated for each grid size and were compared with the range of mainlobe widths within which fall 98 percent of the mainlobe widths (i.e., 1 to 99 percent in the cumulative distribution). A comparison of the ranges of half power mainlobe bandwidths obtained from the 2,000 randomly generated array configurations and the predictive model for each grid size is shown in Figures 9(a) and (b) for 16 and 64-microphone arrays, respectively. Note that the value of grid size on the vertical axis of Figure 9 was determined by the total number of the grid points of a grid (for instance 25 in the case of 5×5 grid). In Figure 9, the ranges of mainlobe widths obtained from the randomly generated arrays are represented by the lighter gray bars, while the range of the mainlobe widths associated with the $\pm 1.5\,\sigma$ deviations of the squared magnitude of the aperture smoothing functions are represented by the darker gray bars for each grid size (note that there are no light bars for the cases of 4 x 4 (16-microphone arrays) and 8 x 8 (64-microphone arrays) since only a single fully-populated array configuration is allowed for those cases). The symbol x within each bar represents the mean values of the mainlobe widths. It can be seen that the lower ends of the ranges and the mean values predicted by the theory agree reasonably well with those obtained from the simulations for larger grid sizes for both the 16 and 64-microphone arrays. For the smaller grid sizes, the mean values of the mainlobe widths are well predicted but the variations of the mainlobe widths were overestimated by the theory. This follows since the variation of the squared magnitude of the aperture smoothing function is overestimated for smaller grid sizes as discussed in subsection 3.1.

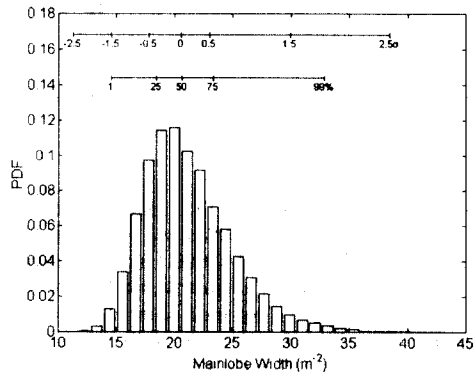

Figure 8: Bar graph of the probability density function for the distribution of the 3 dB-down mainlobe width based on 20,000 16-microphone random arrays generated using segmenting scheme 2 on a 12×12 grid size. The lower of the two horizontal lines plotted above the PDF represents the accumulated percentage of the distribution (data); the upper horizontal line denotes the mainlobe widths that were obtained from corresponding variations from the expected squared magnitude of the aperture smoothing function (theory).

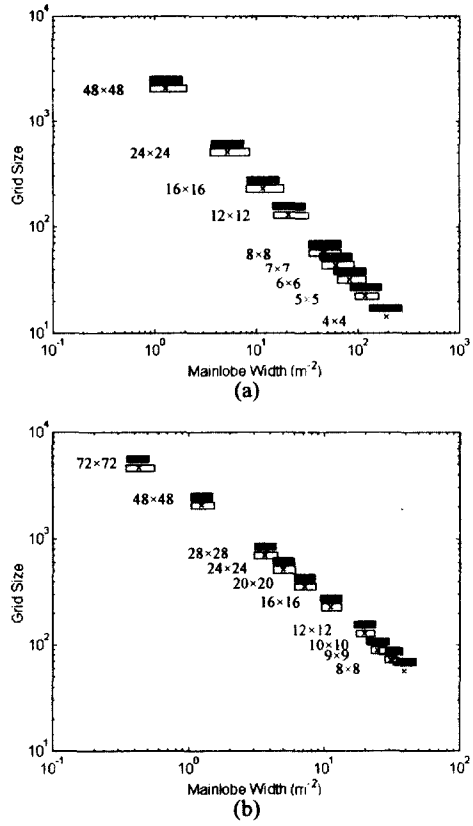

Figure 9: Comparisons between the ranges of the 1-to-99 percent of distributions of 3 dB-down mainlobe widths obtained from various sets of 2,000 randomly generated arrays and the 3-dB down mainlobe bandwidths of the $\pm 1.5\sigma$ variations from the expected squared magnitude of the aperture smoothing functions for different gird sizes. Each pair of bars represents the comparison for each grid size. In each pair of gray bars, the lower, lighter bar denotes the range obtained from simulated data, while the upper, darker bar denotes the range obtained from the model. In each bar, the x's represent the mean values (50% and $\sigma = 0$, respectively). (a) 16-microphone arrays; (b) 64-microphone arrays.

3.4. PROBABILISTIC DISTRIBUTION OF PEAK SIDELOBE LEVELS

Next, an approximate method that can be used to estimate the mean values and the probability distribution of the peak sidelobe levels for randomly generated array configurations is presented. Equations (8) and (9) can only yield the mean values and variances of the sidelobe levels at each wave number and do not directly reveal information about the mean value and the variances of the peak sidelobe levels since the latter, in principle, can occur at all wave numbers except within the mainlobe region. The probability density function of the peak sidelobe levels depends on those functions of level distributions at each wave number in the sidelobe region. Note, however, that no information on the nature of the probability distribution function of the sidelobe levels can be obtained from Equations (8) and (9).

3.4.1 Sidelobe Level Probability Density Functions

In the present work, the probability density function of the sidelobe level distribution was modeled based on the distribution of sidelobe levels obtained from simulations. For two locations in the wave number domain, for both 16 and 64-microphone arrays, the distributions of the sidelobe levels were obtained from 20,000 randomly generated array configurations (segmenting scheme 2, grid spacing 1/11 m). For the 16-microphone array case, the grid size used was 12×12, and the sidelobe levels were evaluated at (k_x, k_z) = (0, -8.64) and (k_x, k_z) = (-31.57, -31.57) (refer to Figure 5 where the variance and the mean levels of the squared magnitude of the aperture smoothing function over the domain are shown). For the 64-microphone array, the grid size used was 24×24, and the sidelobe levels were evaluated at (k_x, k_z) = (0, -4.32) and (k_x, k_z) = (-30.21, -30.21). In each case, the first of these locations is one at which the peak sidelobe occurs in the expected squared magnitude of the aperture smoothing function. The second location is that at which the sidelobe at the lower left corner in the wave number domain occurs. Figures 10(a), (b), (c), and (d) show the probability density functions obtained from the simulations for each case. In the figures, the levels of the sidelobes were represented on a linear scale extending from zero to one where a value of one represents the normalized peak level of the mainlobe at that location.

It can be observed in Figure 10 that the shape of the distributions are not symmetric about their mean values, and that the shapes vary depending on position in the wave number domain as well as on the number of microphones used in the array configurations. An attempt was made to curve fit the sidelobe level distributions obtained from the simulations by using conventional probability density functions. Weibull, Gamma, Exponential, and Beta density functions were tested, and the Weibull density function was found to yield the best fit with the data among the probability density functions tested. The Weibull density function is defined as [11]:

$$f_X(x) = abx^{b-1}e^{-a^b}u(x) \qquad (17)$$

where x is the random variable and $u(x)$ is unity for $x > 0$ and zero otherwise. The two parameters in the Weibull distribution, a and b, are related to the mean, $\overline{X}$, and the variance, σ_X^2, of the random variable, x, as follows:

$$\overline{X} = \frac{\Gamma\left(1+b^{-1}\right)}{a^{1/b}} \tag{18}$$

$$\sigma_X^2 = \frac{\Gamma\left(1+2b^{-1}\right) - \left[\Gamma\left(1+b^{-1}\right)\right]^2}{a^{2/b}}, \tag{19}$$

where Γ denotes the Gamma function. The two parameters a and b are uniquely related to the mean value and the variance by Equations (18) and (19), while the mean values and the variances at arbitrary positions in the wave number domain can be obtained by evaluating Equations (8) and (9). For each of the cases illustrated in Figure 10, the parameters a and b were obtained by using the method described above, and the Weibull density function fittings are represented as solid lines in Figures 10(a), (b), (c), and (d). Good agreement was found in each of the cases considered here, and so it was assumed that the distributions of sidelobe levels at each position in the wave number domain follow the Weibull distribution.

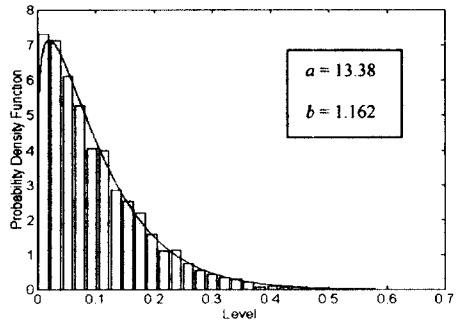

(a)

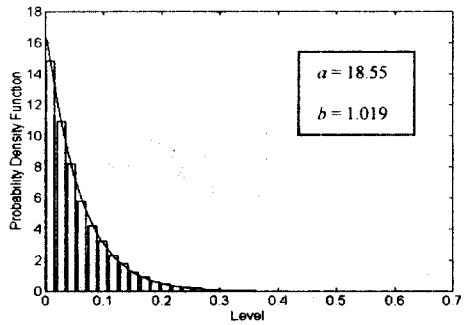

(b)

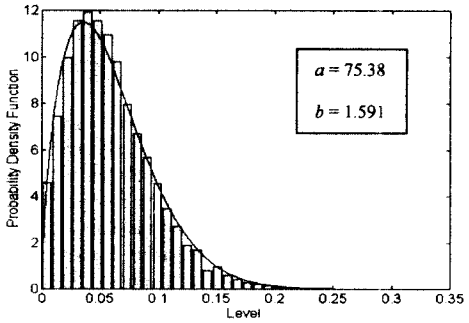

(c)

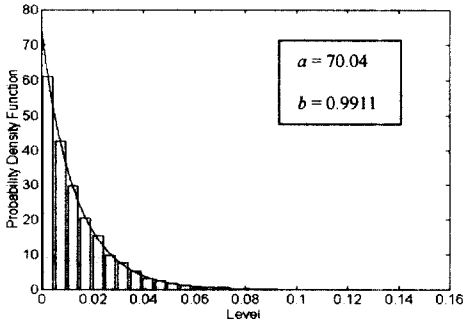

(d)

Figure 10: Plots of the probability density function for the distribution of the sidelobe levels obtained from 20,000 random arrays generated based on segmenting scheme 2. Solid lines are curves fitted based on the Weibull distribution; (a) and (b) are for 16-microphone arrays with a grid size of 12×12; (c) and (d) are for 64-microphone arrays with a grid size of 24×24. Sidelobe levels were evaluated at (a) $(k_x, k_z) = (0, -8.64)$, (b) $(k_x, k_z) = (-31.57, -31.57)$, (c) $(k_x, k_z) = (0, -4.32)$, and (d) $(k_x, k_z) = (-30.21, -30.21)$.

3.4.2 Correlation of Levels at Two Wave Numbers

Recall, however, that the distribution of *peak* sidelobe levels itself may not follow the Weibull distribution since the peak sidelobe does not occur at a fixed position in the wave number domain. The peak sidelobe level can be identified as the maximum level among the levels in the neighborhood of the sidelobe regions where each of the probability distributions of the level was modeled as following a Weibull distribution. In practice, the levels of the squared magnitude of the aperture smoothing function are correlated at neighboring wave numbers and uncorrelated at distant wave numbers. Lo [8] assumed that

the process of determining the peak sidelobe levels could be approximated as determining the maximum level among a finite number of independent events of random variables. The approach followed in the present study was based on the same idea.

Since the number of "independent events" through which the peak sidelobe level is determined would depend on the area in the wave number domain over which a level of the squared magnitude of the aperture smoothing function at a particular wave number has a strong influence, it is of interest to look at the correlation between levels of the function at two different wave numbers. The degree of the correlation between two random variables can be quantitified by the covariance of the two random variables. The covariance is a joint moment and is defined as follows for two random variables, X and Y [10]:

$$\mathrm{cov}[X,Y] \equiv \mathrm{E}[XY] - \mathrm{E}[X]\cdot\mathrm{E}[Y]. \qquad (20)$$

The correlation coefficient is a covariance normalized with respect to the standard deviations of the random variables X and Y: i.e.,

$$\rho_{X,Y} = \frac{\mathrm{cov}[X,Y]}{\rho_X \rho_Y} \qquad (21)$$

where ρ_X and ρ_Y represent the standard deviations of the two random variables X and Y, respectively.

It is perhaps possible that the correlation coefficient relating levels of the squared magnitude of the aperture smoothing function at two wave numbers, $\vec{k}_1$ and $\vec{k}_2$, can be investigated theoretically. However, the derivation of the correlation coefficient relating levels of the squared magnitude of the aperture smoothing function at two wave numbers for the case of random arrays generated based on segmenting scheme 2 is a tedious task, if not actually impossible. Here, the correlation coefficient for the simpler case of segmenting scheme 1 was derived instead, and that result is:

$$\begin{aligned}
\rho_{X,Y} = & [2(M-2)\mathrm{Re}\{\Phi(-\vec{k}_1)\Phi(\vec{k}_2)\Phi(\vec{k}_1-\vec{k}_2) \\
& + \Phi(\vec{k}_1)\Phi(\vec{k}_2)\Phi(-\vec{k}_1-\vec{k}_2)\} + |\Phi(\vec{k}_1+\vec{k}_2)|^2 + |\Phi(\vec{k}_1-\vec{k}_2)|^2 \\
& - 2(2M-3)|\Phi(\vec{k}_1)|^2|\Phi(\vec{k}_2)|^2]/[1+|\Phi(2\vec{k}_1)|^2 \\
& + 2(M-2)|\Phi(\vec{k}_1)|^2 \\
& + 2(M-2)\mathrm{Re}\{\Phi(2\vec{k}_1)\Phi^2(-\vec{k}_1)\} - 2(2M-3)|\Phi(\vec{k}_1)|^4]^{1/2} \\
& /[1+|\Phi(2\vec{k}_2)|^2 + 2(M-2)|\Phi(\vec{k}_2)|^2 \\
& + 2(M-2)\mathrm{Re}\{\Phi(2\vec{k}_2)\Phi^2(-\vec{k}_2)\} - 2(2M-3)|\Phi(\vec{k}_2)|^4]^{1/2}.
\end{aligned} \qquad (22)$$

The correlation coefficient was calculated by using Equation (22) for the case of 16-microphone random arrays having a grid size 12×12 and a grid spacing of 1/11 m. Figure 11 shows the plot of the correlation coefficient evaluated for a fixed $\vec{k}_1$ = (-20, -20) and a varying $\vec{k}_2$. The wave number $\vec{k}_1$ represents one of the peak locations of sidelobes in the expected squared magnitude of the aperture smoothing function. It is shown that the correlation coefficient decreases rapidly as the wave number $\vec{k}_2$ moves away from the wave number $\vec{k}_1$. Also note that an identical peak appears at $\vec{k}_2$ = (20, 20), since the squared magnitude of the aperture smoothing function is symmetric with respect to the origin in the wave number domain. Thus Figure 11 shows that the levels of the squared magnitude of the aperture smoothing function are almost uncorrelated with that at $\vec{k}_1$ = (-20, -20) outside the peaks of the correlation coefficient.

Figures 12(a) and (b) show the 0.05-level contour lines of the correlation coefficient when $\vec{k}_1$ was set to the each of the sidelobes locations of the expected squared magnitude of the aperture smoothing functions: (a) for the case of a 16-microphone array with grid size 12×12; (b) for the case of a 64-microphone array with grid size 24×24 (the grid spacing in all cases was 1/11 m). In the figures, sidelobe peak locations (i.e., excluding the mirror sidelobes) are denoted by x's. For the case of the 64-microphone array shown in Figure 12(b), the central portion of the wave number domain was expanded so that it included as many sidelobe peaks in the k_x and k_z directions as in the case of the 16-microphone array. It can be found from Equation (22) that the relative scales of the contour lines with respect to the spacings between the sidelobe peaks is independent of the grid size. From a comparison of Figures 12(a) and (b), it can also be observed that the relative scale in the sidelobe region are not very sensitive to a change in the number of microphones.

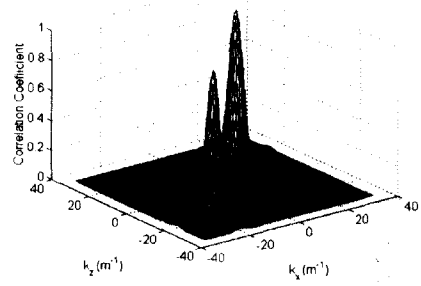

Figure 11: The correlation coefficient between the level of the squared magnitude of the aperture smoothing function evaluated at $\vec{k}_1$ = (-20, -20) and levels evaluated at other wave numbers, $\vec{k}_2$, for 16-microphone random arrays with grid size 12×12.

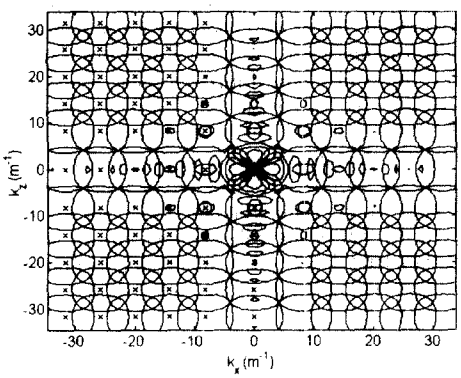

(a)

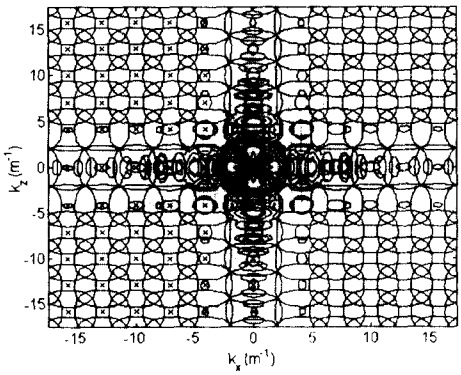

(b)

Figure 12: Contour plots for the 0.05-level correlation coefficient when the wave number, $\underline{k}_1$, was set to locations of sidelobe peaks in the expected squared magnitude of the aperture smoothing functions of (a) a 16-microphone array with a 12×12 grid, and (b) a 64-microphone array with a 24×24 grid.

3.4.3 Probabilistic Distribution of the Peak Sidelobe Levels

Based upon the above observation, it was assumed here that the area of the neighboring region over which a level has correlative influence is independent of the number of microphones. Then, the number of independent occurrences of random levels depends linearly on the number of sidelobes that appear in the sidelobe region of the squared magnitude of the aperture smoothing function. The number of sidelobes depends on the size of the grid (the number of sidelobes can be seen to increase as the grid size increases as shown in Figures 6(a), (b), and (c)).

Here it has been concluded that the probability distribution function, $F_X(x)$, for the random variable, X, the peak sidelobe level, can be modeled in terms of the probability distribution functions for each of the sidelobe levels: i.e.,

$$F_X(x) = \left[\prod_i^{ns} \left\{ F_{X_i}(x) \right\}^{w_i} \right]^{npow} \tag{23}$$

where X_i is the random variable that stands for the levels of the squared magnitude of the aperture smoothing function evaluated at the independent sidelobe peaks of the expected squared magnitude of the aperture smoothing function (points denoted by x's in Figures 12(a) and (b)), *ns* represents the number of independent sidelobes that linearly depends on the grid size, the parameter w_i is the first weighting factor, and *npow* is the second weighting factor.

The probability distribution function $F_{X_i}(x)$ for the level distribution at the i-th sidelobe can be obtained from integration of the probability density function given by Equation (17). The first weighting factor w_i depends on the appearance of the sidelobes that occur on the boundaries or at the corners of the rectangular wave number domain; i.e., it is 1/2 for the case when only half of a sidelobe appears, 1/4 for the case when only a quarter portion of a sidelobe appears, and is unity otherwise. The half weighting factor would be assigned to the sidelobes at a boundary if an odd number of grid points either in the x or z-directions were specified, while the quarter weighting factor would be assigned if the number of grid points in both the x and z-directions were odd. The second weighting factor *npow* would be unity if the correlation coefficient plots at each of the sidelobes were shaped like rectangular columns of unit height and if these columns were assumed to divide the whole wave number domain, except for the mainlobe region, without overlap or gaps.

Since the plot of the correlation coefficient is cone-shaped, as shown in Figure 11, the second weighting factor *npow* should be other than unity. To estimate an appropriate value for the parameter *npow*, a few values of order one were tested. The predicted probability density functions $f_X(x)$ which can be obtained by differentiating $F_X(x)$ in Equation (23) with respect to x were compared with the probability density functions obtained from 20,000 random array configurations for the cases of 16 and 64-microphone random arrays, respectively (12x12 and 24x24 grid sizes respectively and segmenting scheme 2, grid spacing 1/11 m for both cases). The results are shown in Figures 13(a) and (b) for 16 and 64-microphone random arrays, respectively. Values of, 1, 2, 3 and 4 for *npow* were used in the prediction. It can be seen that the shape of the

predicted probability density function is almost independent of the change in the exponent power, and that the predicted distributions agree reasonably well with the shape of the probability density functions obtained from simulations both for 16 and 64-microphone arrays. The predicted probability density function shifted to the right as the power, *npow*, increased, but the amount of shifting was not linearly related to the change in *npow*. For the 16-microphone case, a value of about 3.5 for *npow* yielded a reasonable agreement with the simulations, while a value of 2.0 yielded a better agreement with the simulated data for the case of 64-microphone array. The reason for the difference in the appropriate parameter *npow* for the two cases is not apparent at present. However, fixing the parameter at a value appropriate for one case would not result in serious errors in the prediction for the other case.

In the present study, 2.0 was selected as the parameter, *npow*, and the ranges of the 1 percent to 99 percent levels of the peak sidelobe level distributions (and the associated mean values) that were predicted were compared with those obtained from each set of 2,000 array configurations randomly generated for the cases investigated earlier as shown in Figures 9(a) and (b). The results shown in Figures 14(a) and (b) are for the cases of 16 and 64-microphone arrays, respectively. In those figures, for each grid size, the range of the 1 to 99 percent distributions obtained from the simulated data are shown as the lighter gray bars, while the ranges predicted by using the theory are denoted by the darker gray bars. The mean values of the peak sidelobe levels are represented by x's inside the bars.

For both the 16 and 64-microphone cases, the lower end of the range of the peak sidelobe levels obtained from the simulated data increases as the grid size increases as expected, and the model predicts this tendency with reasonable accuracy. For relatively large grid sizes (i.e., greater than or equal to 8×8 for the case of the 16-microphone array, and 16×16 for the case of 64-microphone array), the theoretical model predicted the 1 percent and the mean levels with errors less than 1 dB. For relatively small grid sizes, the 1 percent and the mean levels are predicted to be larger than those values obtained from the simulations. This also follows from the fact that Equations (8) and (9) overestimate the mean and variances of the squared magnitude of the aperture smoothing function for the case of smaller grid sizes.

It is interesting to note that the microphones can be configured so that an array possesses a lower peak sidelobe level than that of the corresponding fully-populated array when the grid size is slightly increased from that of the corresponding fully-populated array. In Figure 14(b), for the cases of the 9×9, 10×10, and 12×12 grid sizes, it is seen that there exist array configurations that have lower peak sidelobe levels than that of the 8×8 fully-populated array configuration whose peak sidelobe level is denoted by a symbol x in the figure. For the case of the 16-microphone arrays shown in Figure 14(a), a similar phenomenon was observed for the case of the 5×5 grid size where those array configurations are hidden in the non-appearing first one percent of the distribution. In light of the discussion presented in Section 3.2, it is likely that those nearly fully-populated array configurations have smaller mainlobe widths than that of the fully-populated array configuration since they have larger polar moments (see Figure 9(a) for the corresponding ranges of mainlobe widths).

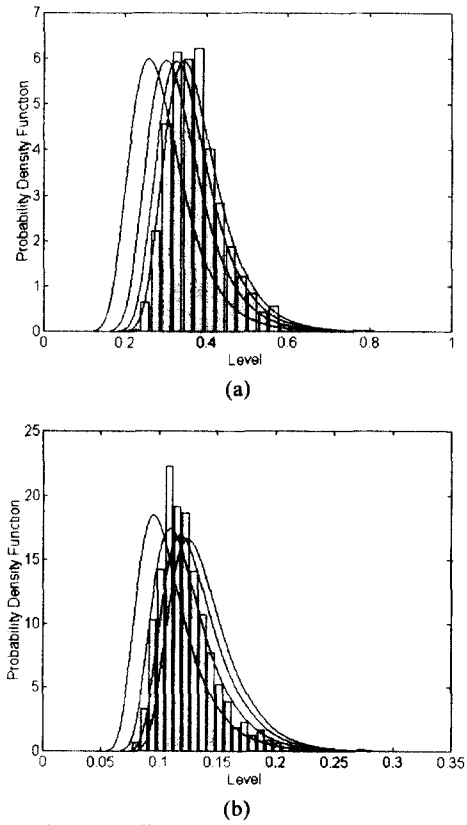

Figure 13: Probability density functions for peak sidelobe level distributions obtained from 20,000 array configurations randomly generated by using: (a) 12×12 grid and 16 microphones; (b) 24×24 grid and 64 microphones. Solid lines represent the prediction with varying the parameter, *npow*, in Equation (23) from 1 to 4 (left to right).

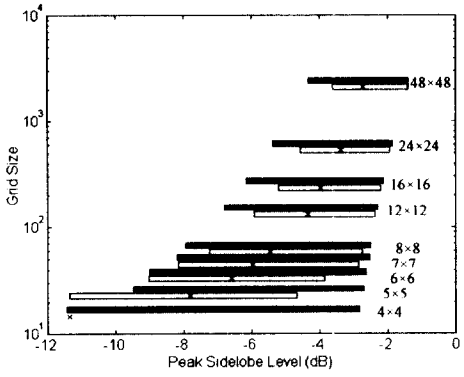

(a)

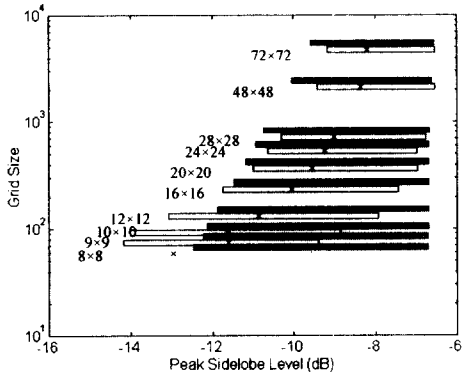

(b)

Figure 14: Comparisons between the ranges of the 1-to-99 percent of distributions of the peak sidelobe levels obtained from 2,000 randomly generated arrays and those predicted by the model for different grid sizes. Each pair of bars represents the comparison for each grid size. In each case, the lower lighter bar denotes the range obtained from simulated data, while the upper darker bar denotes the range obtained from the model. In each bar, the x's represent the mean values; (a) for 16-microphone arrays; (b) for 64-microphone arrays.

3.5. SUMMARY

In Section 3, approximate methods were described that make it possible to estimate the ranges of mainlobe widths and the peak sidelobe levels, respectively, of randomly generated array configurations given a specified number of microphones and a grid size. In particular, the method presented here makes it possible to estimate the lower bound (i.e., the first 1% of the distribution) of the population of possible mainlobe widths without modeling the probability distribution function of the latter since the mainlobe widths of random arrays do not vary much from their mean value. In contrast, to estimate the range of peak sidelobe levels, it was necessary to model the probability distribution function of the peak sidelobe levels since the variance of the latter is in general large. In any particular instance, the grid size and the number of microphones can be optimized by using the predictive tools presented here to obtain random array configurations that meet the requirements for the mainlobe width and the peak sidelobe level before starting a computationally time-consuming search procedure.

For example, given a frequency range of interest, Equation (1) can be used to estimate the maximum grid spacing. Given a requirement for a certain mainlobe width, Equation (9) in combination with Equations (8) and (11) can be used. Given a requirement for a specified peak sidelobe level, Equation (23) can be used (the Weibull parameters a and b at each sidelobe peak can be calculated from Equations (18) and (19)). Simulations that calculate the ranges of the mainlobe width and the peak sidelobe levels of the random array configurations for various grid sizes (provided that the number of microphone is fixed) should be repeated until both the specified peak sidelobe level and the mainlobe width requirements are met. In the simulations, Equation (16) may be used to estimate the initial grid size to test. If it turns out from the simulations that the number of microphone is too small to meet both requirements, simulations can be run for different numbers (i.e., an increased number) of microphones while fixing the grid size at that which meets the mainlobe width specification.

CONCLUSION

In the present work, a predictive model was developed to predict the statistical properties of two-dimensionally sparse arrays in which a number of microphones are randomly positioned on a given grid. The model was found to be able to predict the range of mainlobe widths and the probability distribution of the peak sidelobe levels with reasonable accuracy for the cases of the grid sizes and the number of microphones tested here. For relatively small grid sizes compared with the given number of microphones, the effects of grid size were not negligible and the predictions deviated from the simulated data. To improve the accuracy of the predictions for the case of smaller grid sizes, exact formulae should be derived for the mean and variance of the squared magnitude of the aperture smoothing function of random arrays whose microphones are in practice discretely positioned (while not allowing more than one microphones to be positioned at one point).

From the simulated random array configurations generated based on different grid sizes for two different numbers of microphones, it was observed that the mainlobe width of an array configuration is inversely proportional to the average polar moment of microphone position about the mass center of the array configuration. Also it was observed that array configurations with peak sidelobe levels lower than that of the fully populated array configuration can be obtained by randomly generating array configurations on a grid size that is slightly increased from that of the fully-populated array.

ACKNOWLEDGMENTS

The authors gratefully acknowledge the financial support of Isuzu Motors Ltd. (contract monitor: Dr. Hiroshi Takata).

REFERENCES

1. H. Kook, G.B. Moebs, P. Davies and J.S. Bolton 2000, in press, *Journal of Sound and Vibration*. An efficient procedure for visualizing the sound field radiated by vehicles during standardized passby tests.
2. H. Kook, P. Davies and J.S. Bolton 1999 *SAE Paper* 1999-01-1742, *Proceedings of the 1999 Noise and Vibration Conference*. The design and evaluation of microphone arrays for the visualization of noise sources on moving vehicles.
3. A.T. Moffet 1968 *IEEE Transactions on Antennas and Propagation* **16**, 172-175. Minimum-redundancy linear arrays.
4. E. Panayirci and W.-L. Chen 1995 *Signal Processing* **42**, 319-334. Minimum redundancy array structure for interference cancellation.
5. E. Vertatschitsch and S. Haykin 1986 *Proceedings of the IEEE* **74**, 217. Nonredundant arrays.
6. W.K. Klemperer 1973 in *IEE Conf. on Radar-Present and Future*, Conf. Publ. 105, 74-80. Non-redundant phased array radar.
7. S. Brühl and K.-P. Schmitz 1993 *Proceedings of INTERNOISE 93*, 1311-1314. Noise source localization on highspeed trains using different array types.
8. Y.T. Lo 1964 *IEEE Transactions on Antennas and Propagation* **AP-12**, 257-268. A mathematical theory of antenna arrays with randomly spaced elements.
9. G.B. Moebs 1997 *MSME Thesis, School of Mechanical Engineering, Purdue University*. De-Dopplerization and visualization of sound fields emitted by moving noise sources.
10. D.H. Johnson and D.E. Dudgeon 1993 *Array Signal Processing-Concepts and Techniques*, New Jersey: Prentice Hall.
11. Z. Peyton and JR. Peebles 1987 *Probability, Random Variables, and Random Signal Principles*, New York: McGraw-Hill; second edition.